

Ground penetrating radar imaging of water leaks from buried pipes based on back-projection method

Sevket Demirci^{a,*}, Enes Yigit^b, Ismail H. Eskidemir^c, Caner Ozdemir^{a,d}

^a Department of Electrical-Electronics Engineering, Mersin University, Ciftlikkoy 33343, Mersin, Turkey

^b Vocational School of Technical Sciences, Mersin University, Ciftlikkoy 33343, Mersin, Turkey

^c Faculty of Tarsus Technical Education, Mersin University, Kartal Tepe Mah., Takbas Koyu Mevkii 92, Tarsus, Mersin, Turkey

^d Department of Electrical-Electronics Engineering, Zirve University, Kizilhisar 27260, Gaziantep, Turkey

ARTICLE INFO

Article history:

Received 23 August 2011

Received in revised form

13 December 2011

Accepted 26 December 2011

Available online 3 January 2012

Keywords:

Ground penetrating radar

Water leak detection

Back-projection imaging

ABSTRACT

In this paper, the application of ground penetrating radar (GPR) imaging for detecting the water leaks from buried pipes is examined. Experimental water leakage conditions for a shallowly buried plastic pipe are realized within the laboratory sand and outdoor soil mediums. The successive B-scan GPR measurements of the mediums are performed at various time instants while the water is leaking out of the pipe. The corresponding time-series B-scan images are reconstructed using the back-projection algorithm that we have specifically formulated for the subsurface GPR imaging applications. The signatures of the leak regions are then assessed by both direct interpretation of the resultant images and application of change detection procedures. The obtained results demonstrate the capability of GPR for locating the sources of the leaks accurately.

© 2011 Elsevier Ltd. All rights reserved.

1. Introduction

The loss of water due to leakages within the water distribution networks constitutes a serious problem. According to numerous reports, a substantial amount of water is being lost every day through the leaks within the water distribution systems [1]. Obviously, detecting and locating the sources of these leaks would yield significant water savings. For this purpose, various techniques such as acoustic, infrared, thermography, tracer gases and ground penetrating radar (GPR) have been used for the localization of leaks in water-pipe systems. Among these, GPR that has been recently investigated through quite a number of studies seems to be the most promising method especially for detecting leakages from plastic pipes [2–11]. Principally, electromagnetic (EM) signatures of the leak regions would manifest themselves in GPR images either as void regions or distorted pipe shapes. The sources of the leaks can then be located through the direct interpretation of the GPR images. Since imaging plays a critical role in achieving an efficient detection of the leaks, the performances of various GPR imaging algorithms should be tested on real leakage data.

Synthetic aperture imaging methods commonly used in GPR applications can be generally categorized into two classes;

namely the back-propagation and the back-projection methods. In the literature, the former class is formulated through various algorithms including the Kirchhoff wave-equation [12], the phase-shift method [13], the finite-difference method [14] and the frequency-wavenumber algorithm [15–17]. The latter class is formulated through the geometrical approach and includes the diffraction summation (the time-domain correlation or the matched-filtering) [18,19] and the back-projection [20–25] algorithms. Each of these techniques has advantages and also shortcomings. The back-projection algorithm in particular was originally developed for medical imaging [26] and offers some specific features. First, the algorithm does not require a straight line type synthetic aperture during the data collection since each range (depth) profile is processed individually. This sequential processing means that the imaging process can begin before acquiring the entire synthetic aperture data, which makes the algorithm more suitable for real-time applications. Second, the specific subsections of the region to be imaged can be easily selected to investigate these subsections more closely. In applications where the approximate location of the target is known a priori or detected by a single depth measurement, the detailed image of the region around this target can be easily formed by the algorithm.

Within this framework, the objective of this paper is to assess the value of GPR in detecting the water leaks from the buried plastic pipes. For this task, an experimental scaled-down model of the real leakage conditions was constructed within the shallow depths of the laboratory and the outdoor soil environments.

* Corresponding author. Tel.: +90 324 361 0001 x7163; fax: +90 324 361 0032.

E-mail addresses: sdemirci@mersin.edu.tr (S. Demirci), enesyigit81@mersin.edu.tr (E. Yigit), ieskidemir@mersin.edu.tr (I.H. Eskidemir), cozdemir@mersin.edu.tr (C. Ozdemir).

Assuming that the pipeline routes are generally known a-priori, the B-scan measurements along the longitudinal direction of the leaky pipe were taken at various time instants. The acquired time-series B-scan data were then processed to locate the leak region. Although our main focus was to infer whether the leaks can be judged directly from the B-scan images, some change detection procedures were also investigated to aid the detection process. Due to its advantages mentioned above, the back-projection algorithm that is specifically adapted to near-field GPR imaging applications was used for the image reconstruction. The obtained results indicate that the sources of the leaks can be located by interpreting the void regions of the B-scan images. Besides, the results also demonstrate that it may be difficult to easily discern the void regions in the images for a complex leakage environment. For this case, two different change detection procedures namely, the complex subtraction [27] and the wavelet-based semblance analysis [28] are shown to provide an additional insight to the leak detection problem.

The organization of the paper is as follows: In the next section, the formulation of the near-field back-projection imaging algorithm is derived for the two-dimensional (2D) monostatic GPR set-up that is based on a stepped-frequency continuous-wave radar (SFCWR) system. Experimental results for the leakage detection problem are presented in the third section. The discussions and the comments are given in the concluding section.

2. GPR imaging geometry and the back-projection algorithm

The B-scan geometry for our 2D monostatic GPR application is shown in Fig. 1a. A radar antenna is located at a height of h from the ground surface and transmitting a wide-band waveform at each discrete point of m along the synthetic aperture of length L . The relative permittivity of the subsurface medium is ϵ_r and the reflectivity distribution of the scatterers within the desired scene is represented by $g(x,z)$.

2.1. Range profile generation

A single static measurement on the synthetic aperture is first considered. The transmitted waveform is the single burst of a SFCWR as illustrated in Fig. 1b. As shown from the figure, the frequencies of the single-frequency subpulses within the burst are incremented with a fixed value attaining a larger effective bandwidth of B . Each subpulse has the duration of τ and the time interval between pulses is adjusted according to the desired unambiguous range. Assuming that the starting frequency is f_0 and the frequency resolution is Δf , then the frequency of the n th subpulse can be expressed as:

$$f_n = f_0 + (n-1)\Delta f \quad 1 \leq n \leq N \quad (1)$$

The frequency response of the illuminated subsurface is then acquired by measuring the backscattered field for each of the

stepped-frequencies. The phase lag ϕ_n of this echo signal from the single point scatterer located at (x_0, z_0) for the transmitted frequency of f_n is given as:

$$\phi_n = \frac{-4\pi f_n r_m}{v} \quad 1 \leq n \leq N \quad (2)$$

where r_m is the range from an instantaneous antenna platform location to the point (x_0, z_0) and v is the velocity of the EM wave within the subsurface medium. The corresponding measured data at the m th synthetic aperture position can be expressed as:

$$E_m(f_n) = g(x_0, z_0) \exp\left(-j \frac{4\pi f_n r_m}{v}\right) \quad 1 \leq n \leq N \quad (3)$$

The frequency variable is related with the radial spatial frequency k_r , which can be defined for the two-way propagation as $k_r = 4\pi f/v$. So, Eq. (3) can also be represented as below:

$$E_m(k_{r,n}) = g(x_0, z_0) \exp(-jk_{r,n} r_m) \quad 1 \leq n \leq N \quad (4)$$

The measured field data for a continuous distribution of scattering targets can then be obtained by summing all the responses due to each individual scatterers as:

$$E_m(k_{r,n}) = \int_{-\infty}^{\infty} \int_{-\infty}^{\infty} g(x, z) \exp(-jk_{r,n} r_m) dx dz \quad 1 \leq n \leq N \quad (5)$$

Representing the collected spatial frequency data sequence $E_m(k_{r,n})$ as $E_m(k_r)$, the corresponding time-domain signal $e_m(t)$ at the m th synthetic aperture position can be obtained by taking the one-dimensional (1D) inverse Fourier transform (IFT) of $E_m(k_r)$. Also noting that the linear relationship $r = vt/2$ between time t and range r can be taken under the assumption of constant velocity v , the range profile $e_m(r)$ can be predicted accordingly.

2.2. Imaging using the back-projection algorithm

The frequency-diverse static measurement explained in the previous section is known as the A-scan measurement [29], which gives the depth-profile of the scatterers within the subsurface environment. In order to resolve the targets at different cross-range positions, the illumination angle of the subsurface scene has to be changed with respect to the antenna platform. This can be achieved by conducting a series of A-scan measurements on the straight synthetic aperture; i.e., the B-scan measurement [29]. The variation of the relative distance between the antenna platform and the subsurface scene throughout the B-scan measurement results in a phase modulated received signal. Then, these phase modulated signals can be coherently summed up to obtain the images with high cross-range resolutions. This procedure is commonly known as the ‘‘synthetic aperture processing’’ and implemented in numerous imaging applications by many researchers [30]. In this section, the formulation of the back-projection imaging algorithm will be derived for the synthetic aperture processing of the 2D GPR measurement data.

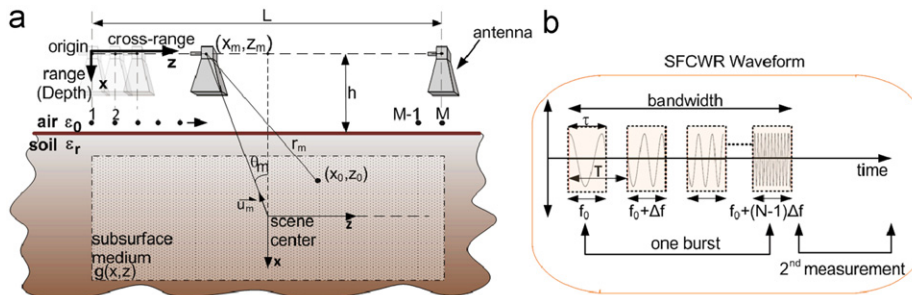


Fig. 1. (a) B-scan geometry of the 2D monostatic GPR application. (b) Illustration of SFCWR waveform.

Referring to geometry depicted in Fig. 1a, let us consider that the antenna is moving along a straight path parallel to the cross-range axis z . The instantaneous location of the antenna platform at (x_m, z_m) is defined by a unit vector \vec{u}_m pointing from the scene center towards this location. The corresponding observation angle at this location is represented by θ_m , which is the angle between the unit vector \vec{u}_m and the range axis x . As shown from Eq. (5), at each measurement point m or corresponding observation angle θ_m , the SFCWR provides the spatial frequency data, which can be rewritten to reflect its observation angle dependency as follows:

$$E_{\theta_m}(k_r) = \int_{-\infty}^{\infty} \int_{-\infty}^{\infty} g(x, z) \exp(-jk_r r_m) dx dz \quad (6)$$

The range profile of the illuminated scene can be found by applying 1D IFT to Eq. (6) and can be mathematically expressed as:

$$e_{\theta_m}(r) \equiv \text{IFT}\{E_{\theta_m}(k_r)\} = \int_{-\infty}^{\infty} \int_{-\infty}^{\infty} g(x, z) \delta(r_m - r) dx dz \quad (7)$$

Eq. (7) is also known as the Radon Transform of the scene, which represents the scene's projection onto the 1D range profile function for the particular observation angle θ_m . The derivation of the back-projection algorithm starts with considering the IFT expression of the reflectivity function $g(x, z)$ given in Cartesian coordinates as:

$$g(x, z) = \int_{-\infty}^{\infty} \int_{-\infty}^{\infty} G(k_x, k_z) \exp[j(k_x x + k_z z)] dk_x dk_z \quad (8)$$

where $G(k_x, k_z)$ is the 2D FT of $g(x, z)$. Since the spatial frequency data samples are collected along the polar radius, Eq. (8) can be modified to be rewritten in the polar coordinates (k_r, θ_m) as follows:

$$g(x, z) = \int_{-\pi}^{\pi} \int_0^{\infty} G(k_r, \theta_m) \exp(jk_r r_m) k_r dk_r d\theta_m \quad (9)$$

At this point, the projection-slice theorem [31] is used to relate the target's FT $G(k_x, k_z)$ to the available measured data $E_{\theta}(k_r)$. For the 2D space, the theorem basically states that 1D FT of the projection at the angle θ represents the slice of the 2D FT of the projected (original) scene at the same angle; i.e., $E_{\theta}(k_r) \equiv G(k_r, \theta)$. Hence, the sampled representation of $G(k_x, k_z)$ can be obtained from the FT of the projections $E_{\theta}(k_r)$ measured at various observation angles. Using this principle, Eq. (9) can be written as given below.

$$g(x, z) = \int_{-\pi}^{\pi} \left[\int_0^{\infty} E_{\theta_m}(k_r) \exp(jk_r r_m) k_r dk_r \right] d\theta_m \quad (10)$$

The bracketed integral in Eq. (10) can be regarded as the 1D IFT of a function $Q_{\theta_m}(k_r) = E_{\theta_m}(k_r) k_r$ evaluated at r_m . Defining $q_{\theta_m}(r)$ as the IFT of this function, Eq. (10) can be represented as:

$$g(x, z) = \int_{-\pi}^{\pi} q_{\theta_m}(r_m) d\theta_m \quad (11)$$

Eq. (11) is the final focused image of the 2D filtered back-projection algorithm. For the SFCWR system, the implementation of the algorithm can be summarized as follows:

- 1) Multiply the acquired spatial frequency data $E_{\theta_m}(k_r)$ with k_r .
- 2) Take 1D IFT to obtain $q_{\theta_m}(r)$.
- 3) For each pixel location in the image, calculate the corresponding range value r_m and obtain its $q_{\theta_m}(r_m)$ value through any interpolation scheme.
- 4) Add interpolated values to $g(x, z)$.
- 5) Repeat steps 1 thru 4 for all the observation angles.

While implementing the above algorithm, various considerations should be taken into account to improve the imaging procedure: First, a zero padding operation can be readily applied

to the frequency data to facilitate the subsequent interpolation step in the range domain. Second, if the exact ranges of the pixel locations are taken in the 3rd step of the algorithm, then the algorithm compensates the wave-front curvature effects. Hence, the algorithm can be conveniently applied to the near-field GPR scenarios. Third, the effect of antenna's finite beamwidth can also be incorporated in the 3rd step of the algorithm. Since the antenna illuminates some restricted subsurface region due to finite width of the main beam, the back-projection step can only be applied to the image points, which fall inside this illuminated area. Finally, the refraction of the EM wave at the air-ground interface can be taken into consideration to calculate the range values of the image pixels more precisely in the 3rd step of the algorithm.

3. Experimental results

The detection and localization of water leaks from the buried plastic pipes were investigated through the laboratory and the outdoor soil experiments. For both experiments, scenarios that reflect the real leakage conditions were realized as illustrated in Fig. 2. A plastic pipe with a diameter of 5 cm was first drilled to have a small hole of 2 mm in diameter to facilitate the water leakage. This pipe is then buried at a shallow depth for both experiments. As shown from the figure, one end of the pipe was kept above the ground to be able to continuously add water into the pipe while the other end of the pipe is sealed. From the time we started putting water into the pipe, successive B-scan measurements of the subsurface medium were acquired at different time instants. The objective of these experiments was to investigate the effect of increasing water quantity of the subsurface medium and observe the change in the radar image of the subsurface region via the time-series B-scan images. The images were constructed using the back-projection algorithm as explained in the previous section.

3.1. Laboratory results

For laboratory measurements, a wooden pool with a size of 190 cm \times 100 cm \times 80 cm was constructed and filled with the dry sand. A plastic pipe was then placed at the depth of 27 cm from the sand's surface. Immediately after the leakage was started, a total of 8 B-scan experiments were performed at 5 cm above the surface and along the pipe for various time instants. For referencing purposes, the measurement data for the empty pipe were also acquired before these 8 B-scan experiments. The scan times and the water supplements are given in Table 1. For each B-scan, the synthetic aperture length of 110 cm with 56 equally spaced points and the frequency band between 4.5 and 6.5 GHz with 201 discrete frequency steps were used. The relative electric permittivity of the sand over this range of frequencies was measured to be nearly constant at 2.43. For the B-scans, quasi-monostatic

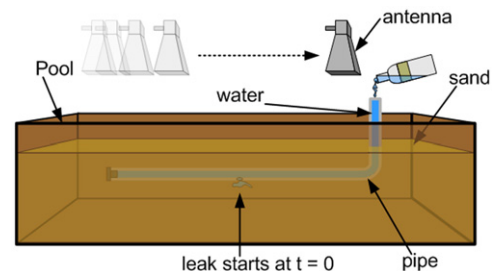


Fig. 2. Geometry for the water leak detection using B-scan measurement.

operation was selected such that two identical rectangular horn antennas were put aside for transmit and receive.

After processing the collected data set via the presented back-projection algorithm, the imaging results for different time instants were obtained as shown in Fig. 3. The plastic pipe is clearly identified in the reference image of Fig. 3a. The sand surface and the bottom of the pool can also be visible within the selected dynamic range. We also put a reference metal target between the pipe and the pool's bottom that can be easily observed on the right side of Fig. 3a. Just after filling the pipe with water; however, the EM reflection from the water is more pronounced such that the reflections from the sand surface, the pool's bottom and the reference target are fainter as shown in Fig. 3b. The image that is obtained by taking a B-scan 5 min after

the start of leakage is presented in Fig. 3c. In this image, some minor discrepancies with respect to the previous image can be observed especially in the regions below the leak location where the water content of the medium was changing as the time passed. This dynamic situation around the leak location becomes more noticeable from the figures between Fig. 3d and i that demonstrate the images of increasing water content inside the subsurface medium. The observed phenomenon throughout these images is that, as the water content of the sand increases, the distortion of the pipe shape at the leak location becomes more explicit and the void region beneath the leak location gets larger. Since the EM wave attenuates as it passes from the water-saturated region, the reflections from the scatterers beneath this region get weaker forming voids within the GPR images. As time passes longer and the amount of water that leaks into the soil increases, the voids in the GPR image become larger and provide the required valuable information about the location of the leak region.

To further understand the effect of increasing quantity of the water in the subsurface medium on the EM reflections, the complex subtraction between the consecutive images was also applied. The difference images are obtained by subtracting the focused image data from the subsequent ones as shown in Fig. 4. As observed from Fig. 4b and c, the leak region clearly shows up as the strong marks. This is due to the fact that the difference image easily puts forward the dynamic part of the region while the static regions are filtered out thru the subtraction process. Although direct imaging gives the sufficient information about the leak

Table 1
Scan details for the laboratory experiment.

Scan time (min)	Actions
$t < 0$	Empty pipe, B-scan is performed
$t = 0$	Water added, B-scan is performed
$t = 5$	B-scan is performed
$t = 15$	B-scan is performed
$t = 25$	Water added, B-scan is performed
$t = 45$	B-scan is performed
$t = 50$	B-scan is performed
$t = 60$	Water added, B-scan is performed
$t = 165$	B-scan is performed

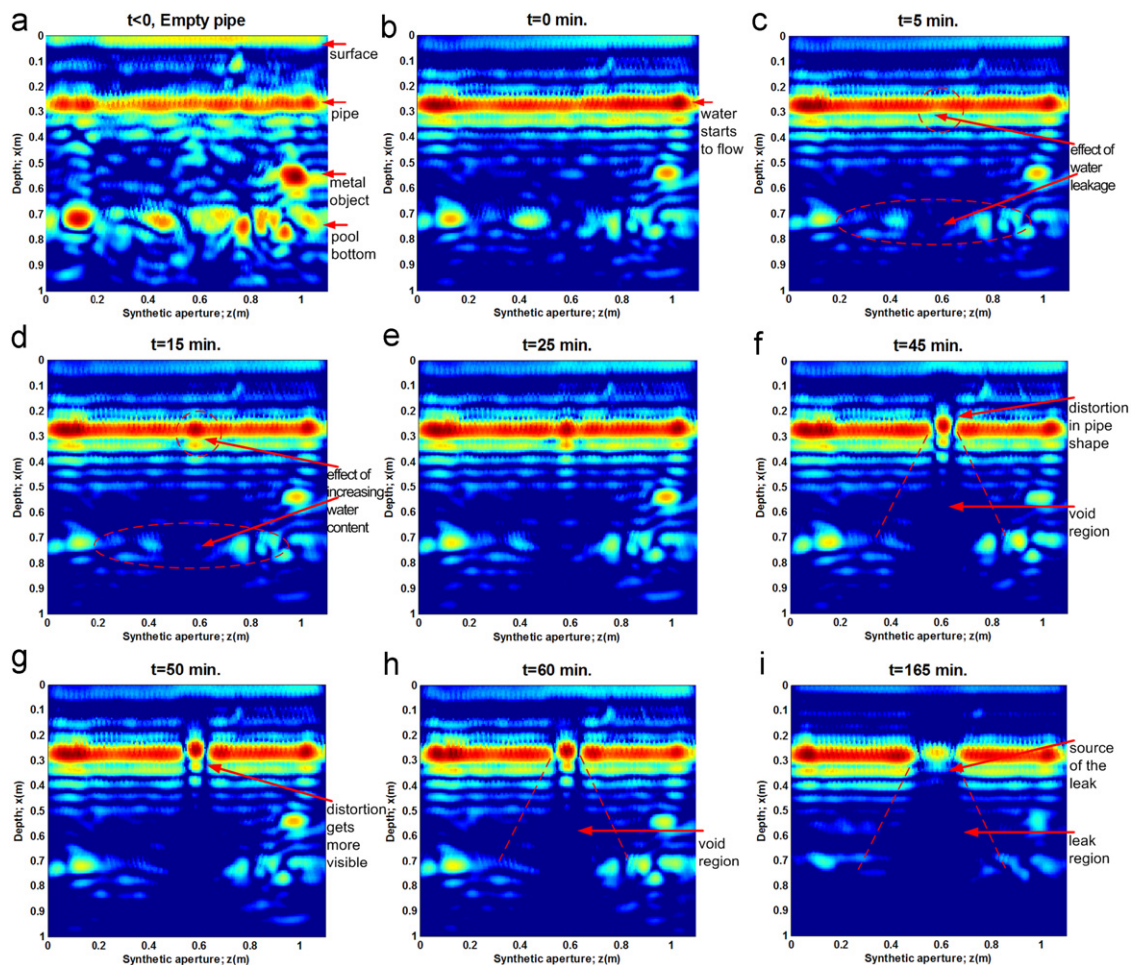


Fig. 3. GPR images of the laboratory experiment for different times: (a) empty pipe, (b) $t = 0$ min, (c) $t = 5$ min, (d) $t = 15$ min, (e) $t = 25$ min, (f) $t = 45$ min, (g) $t = 50$ min, (h) $t = 60$ min and (i) $t = 165$ min (all images are displayed within the dynamic range of 25 dB).

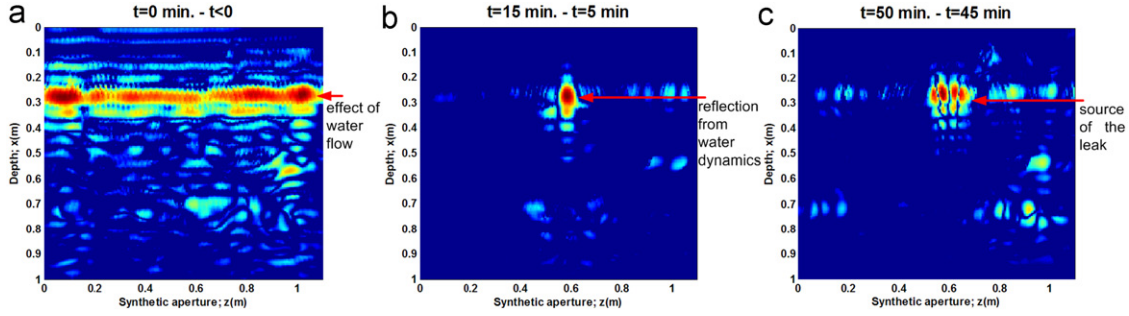


Fig. 4. Differences of GPR images between: (a) $t=0$ min and empty pipe, (b) $t=15$ min and $t=5$ min and (c) $t=50$ min and $t=45$ min (all images are displayed within the dynamic range of 25 dB).

Table 2

Scan details for the first outdoor experiment.

Scan time (min)	Actions
$t < 0$	Empty pipe, B-scan is performed
$t = 0$	Water added, B-scan is performed
$t = 10$	Water added, B-scan is performed
$t = 20$	Water added, B-scan is performed
$t = 30$	Water added, B-scan is performed

location for this idealistic laboratory conditions, the difference images might also be of value for more challenging situations in estimating the location of the leak.

3.2. Outdoor results

3.2.1. Outdoor experiment 1

For the first outdoor experiment, a GPR test-bed was constructed in a partly homogeneous outdoor soil environment. The same plastic pipe that was used in the laboratory experiment was buried at the depth of 10 cm from the ground surface. First, a reference B-scan measurement of the empty pipe was performed. Afterwards, a total of 4 consecutive B-scan experiments at equal time intervals were conducted while adding water into the pipe as given in Table 2. For each scan, the synthetic aperture of length 64 cm with 33 discrete spatial points and the frequency band between 0.8 and 5 GHz with 301 discrete frequency steps were used. The data were collected in the quasi-monostatic operation by the help of two double-ridged horn antennas.

The B-scan GPR imaging results for different time instants were obtained as shown in Fig. 5. The region of the leak can be deduced again from the void region, which is visible through the images (see Fig. 5c–e). Also, we provide the difference images of the consecutive B-scan measurements in Fig. 6.

3.2.2. Outdoor experiment 2

To determine the practical limitations of the detection scheme, a second outdoor experiment was conducted for a relatively more inhomogeneous soil environment when compared to the first outdoor experiment. The initial water content of the sampled soil medium was measured by the gravimetric method [32] and found as 16.74%. To resemble the conditions of a major leakage situation, the 5 cm diameter pipe was drilled to have three adjacent leakage holes each of which has a 2 mm diameter. The pipe was then buried at a depth of 30 cm from the ground surface. Sample photographs from these preliminary stages of the experiment are shown in Fig. 7. Unlike previous experiments, a constant flow of water within the pipe was then maintained as illustrated in the conceptual diagram of the experiment shown in Fig. 8. Also, only

two B-scan measurements were performed to provide a practical detection scheme. The first measurement data were collected 25 min after the starting time of the leakage so that the water content of the soil has been risen to a level that was comparable to a real world scenario. The second measurement was conducted 15 min later than the first one. For both measurements, the scanning aperture was 1.2 m long with 2 cm equally spaced intervals. The frequency of the monostatic radar set-up was altered from 3 to 5 GHz with 151 uniformly sampled discrete points. The leaks were known to be located at around 60 cm away from the beginning of the scanning aperture.

The reconstructed B-scan images with a range resolution of 7.5 cm are drawn in Fig. 9. It is seen from the images that the pipe can be identified at a depth of 60 cm from the antenna despite the fact that reflection from the ground surface is quite high. As shown from the Fig. 9a and b; however, it could not be possible to discern the expected void phenomenon within the selected dynamic range of the images. Hence, a wavelet-based semblance analysis technique [28] was applied to the time-dependent A-scan data (range profile) of each sampling point on the scanning aperture to retrieve the information about the leak location. The operation of the technique can be briefly explained as follows:

- i) Take any two raw range profiles $e_1(r)$ and $e_2(r)$ of the investigated aperture position that are measured at different time instants.
- ii) Take the complex continuous wavelet transform (CWT) of the each range profile.
- iii) Calculate the cross-spectrum using

$$\text{CWT}_{1-2} = \text{CWT}\{e_1(r)\} \times \text{CWT}^*\{e_2(r)\} \quad (12)$$

- iv) Calculate the phase angle θ of the cross-spectrum CWT_{1-2} .
- v) Obtain the semblance using

$$S = \cos(\theta) \quad (13)$$

The calculated semblance values S will then give a measure of the phase correlation between the two range profiles $e_1(r)$ and $e_2(r)$ for the different scales of the used wavelet, where values close to “-1” indicate high negative correlation, “0” indicate no correlation and “1” indicate high positive correlation [28].

The technique was implemented using 40 scales of complex Morlet wavelet [33] and applied to each range profile pair that was measured on the same scanning aperture position. Here, only the results for some selected aperture positions are given as shown in Fig. 10. First, it is observed throughout the images that the semblance values calculated for the depths ranging from 0 cm to 60 cm indicate high positive correlation for almost all

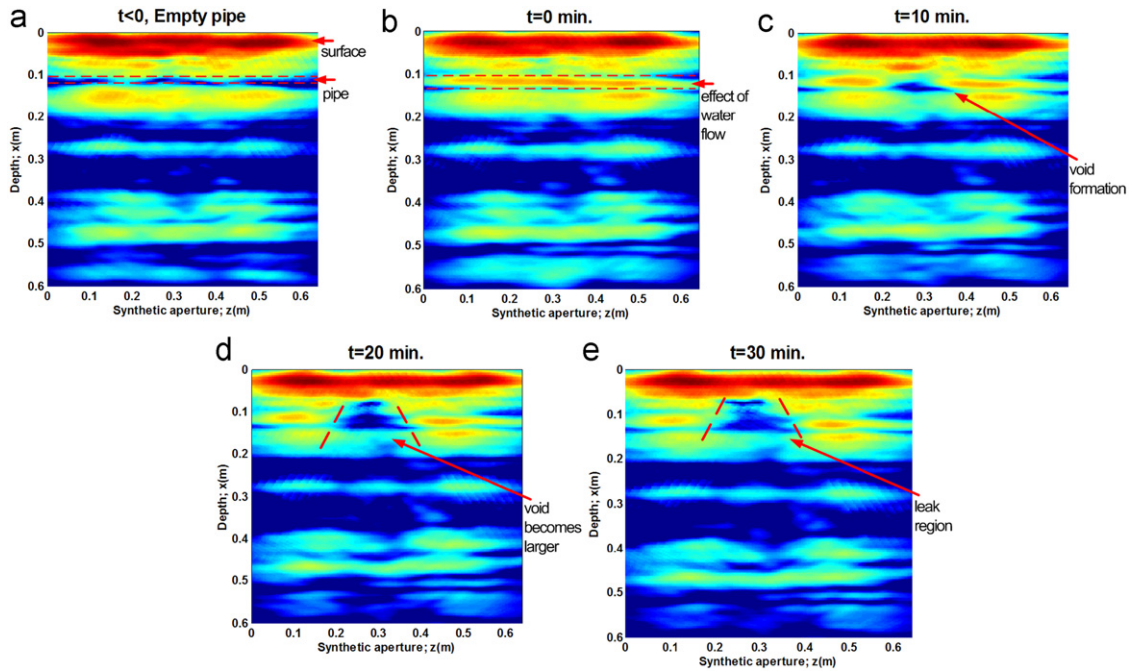


Fig. 5. GPR images of the first outdoor experiment for different times: (a) for empty pipe, (b) $t=0$, (c) $t=10$ min, (d) $t=20$ min and (e) $t=30$ min (all images are displayed within the dynamic range of 25 dB).

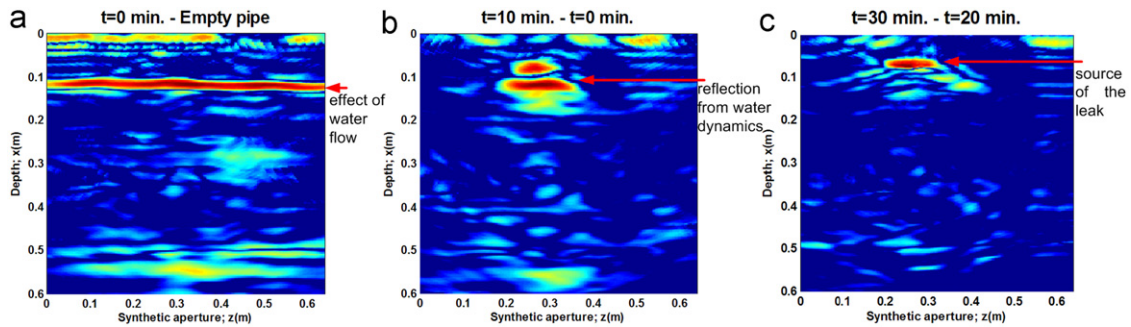


Fig. 6. Differences of GPR images between: (a) $t=0$ min and empty pipe, (b) $t=10$ min and $t=0$ min and (c) $t=30$ min and $t=20$ min (all images are displayed within the dynamic range of 25 dB).



Fig. 7. Sample photographs from the preliminary stages of the second outdoor experiment; (a) pipe with three leaks, (b) burial of the pipe and (c) B-scan measurement set-up.

wavelength scales. This is an expected behavior since there is no any dynamic event within the range from the antenna to the pipe's upper surface. Second, the images involve semblance values that deviate from the high positive correlation value especially for the depths below 60 cm and for the wavelength scales up to 20. It is worth noting here that these deviations occurring at the depth of nearly 70 cm and beyond can be attributed to the water flow within the pipe and to the leakage

of water into the soil, respectively. If the images for the different aperture positions are compared, the images at 58, 60 and 62 cm are shown to have the most drastic deviations and comprise large number of semblance values tending towards the high negative correlation value. This is an important result for the detection mission simply because leaking holes were actually located at around the aperture position of 60 cm. Furthermore, the images for the positions near by the leaking holes are also observed to

possess considerable deviations from high positive correlation. This definitely indicates that the beamwidth of the antenna covers the leak region in the measurements of these positions, thereby producing little changes between the range profiles. Contrary to this case, the images for 14 and 106 cm represent

the results of the measurements in which the leak region is almost out of the antenna beamwidth, hence representing positively correlated range profiles. Briefly, the results demonstrate that the detection of the leak region can be efficiently succeeded by determining the aperture positions whose semblance analysis results show dominant negative correlation signatures.

4. Conclusion

This paper has presented some experimental results for the GPR-based water leak detection problem. Since in principle, leaking water from the pipe shows up as void regions and/or distorted pipe signatures in the B-scan GPR images, the primary focus was to test the validity of this principle through straightforward imaging of experimental leakage data. As being critical to this objective, the near-field back-projection imaging algorithm was derived for the 2D monostatic GPR geometry. Then, the time-series B-scan data from the experimental scaled-down models of the real leak detection application were acquired and processed for different soil cases.

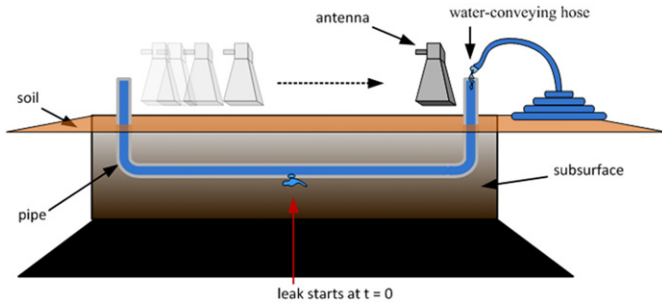


Fig. 8. Conceptual diagram of the leak detection measurements employed in the second outdoor experiment.

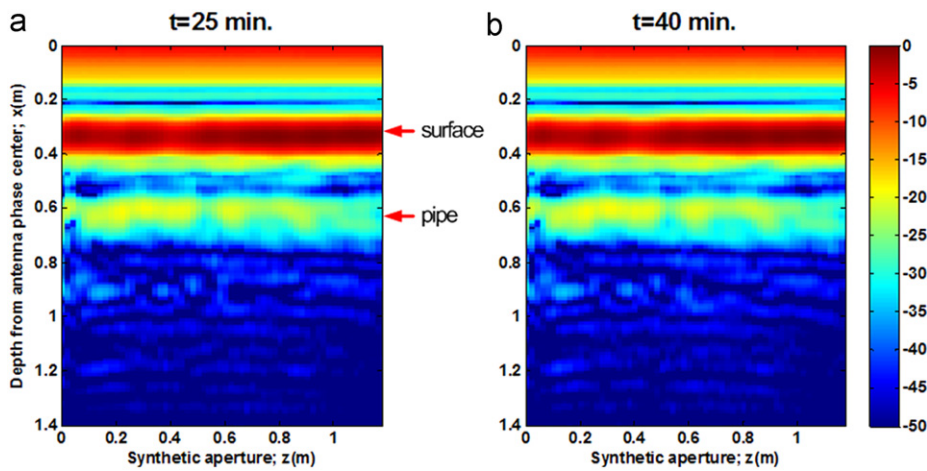


Fig. 9. GPR images of the second outdoor experiment for: (a) $t=25$ min and (b) $t=40$ min.

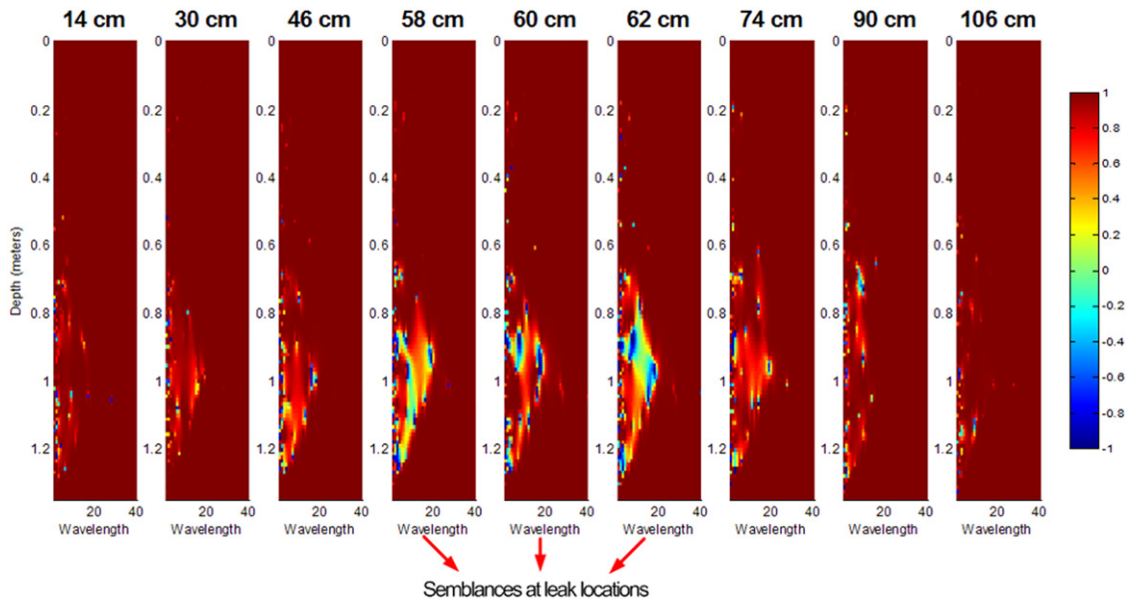


Fig. 10. Wavelet-based semblance analysis results for the second outdoor experiment. Images represent the phase correlation between the two range profiles of the investigated aperture position, which are taken at $t=25$ min and $t=40$ min.

The results from the presented experiments show that detection through voids highly depends on the investigated medium and the radar system parameters. To be more specific, the reflections beneath the leak regions become comparatively weaker than the ones from the surrounding soil medium for most homogeneous soils. Then, it could be possible to detect the void regions in the B-scan images as demonstrated by our laboratory and first outdoor experiment results. Besides, it may not be possible to observe the void phenomenon for more inhomogeneous soils such as the one used in our second outdoor experiment. In this study, we proposed the wavelet based semblance analysis technique for such cases to successfully estimate the location of the leak region. The presented results express that the detection of the leaks can be achieved by displaying the phase correlation between two distinct range profiles of each scanning aperture position.

The imaging-based detection method can be readily applied to the water distribution networks that are shallowly buried beneath the surface. When the pipes are located deep within the surface, either the moisture of the soil and/or the inhomogeneities within the soil may not provide sufficient signal power levels above the noise floor, which may put a limit on the success of the procedure. On the other hand, we found that the wavelet-based semblance analysis technique provides a very efficient change detection scheme for identifying any change within the selected region of interest. Further analysis needs to be applied especially for leakage problems of deeper regions.

It is also important to note that our B-scan measurements were conducted along the longitudinal direction of the pipe, which assumed that the route of the pipe is known a priori. In fact, the pipeline distribution plan, which has a piece-wise linear line geometry in three-dimensional (3D) space is available in most city municipalities.

Acknowledgments

This work is supported by the Scientific and Research Council of Turkey (TUBITAK) under grant no: EEEAG-104E085 and Mersin University's Scientific Research Fund under grant no: BAP-FBE EEM (İHE) 2009-1. The authors are grateful to Mersin Trakya Cam A.S. for providing the sand material and Department of Mechanical Engineering of Mersin University for providing laboratory facilities for the conducted experiments. The authors are also thankful to Dr. Korkut Yegin of Yeditepe University for valuable discussion and to Betül Yılmaz for her help during the experiments.

References

- [1] Hunaidi O, Chu W, Wang A, Guan W. Detecting leaks in plastic pipes. *J Am Water Works Assoc* 2000;92:82–94.
- [2] Hunaidi O, Giamou P. Ground-penetrating radar for detection of leaks in buried plastic water distribution pipes. In: *Proceedings of the Seventh International Conference on Ground Penetrating Radar*, KS-Laurence, 1998, p. 783–6.
- [3] Stampolidis A, Soupios P, Vallianatos F. Detection of leaks in buried plastic water distribution pipes in urban places—a case study. In: *Proceedings of the Second International Workshop on Advanced GPR*, Delft-Netherlands, May 14–16, 2003, p. 120–4.
- [4] Eyuboglu S, Mahdi H, Al-Shukri HJ. Detection of water leaks using ground penetrating radar. In: *Proceedings of the Third International Conference on Applied Geophysics*, Orlando-FL, December 8–12, 2003.
- [5] Nakhkash M, Mahmood-Zadeh MR. Water leak detection using ground penetrating radar. In: *Proceedings of the Tenth International Conference on Ground Penetrating Radar*, Delft-Netherlands, June 21–24, 2004, p. 525–8.
- [6] Kim SW, Kim SY. Comparison of FMCW and pulse type GPR for water leakage detection. In: *Proceedings, IEEE International Geoscience and Remote Sensing Symposium* 2005, Seoul, Korea, July 25–29, 2005, vol. 7, p. 4596–9.
- [7] Hyun SY, Jo YS, Oh HC, Kim SY, Kim YS. The laboratory scaled-down model of a ground-penetrating radar for leak detection of water pipes. *Meas Sci Technol* 2007;18:2791–9.
- [8] Bimpas M, Amditis A, Uzunoglu N. Design and implementation of an integrated high resolution imaging ground penetrating radar for water pipeline rehabilitation. *Water Resour Manag* 2011;25(4):1239–50.
- [9] Bimpas M, Amditis A, Uzunoglu N. Detection of water leaks in supply pipes using continuous wave sensor operating at 2.45 GHz. *J Appl Geophys* 2010;70(3):226–36.
- [10] Crocco L, Prisco G, Soldovieri F, Cassidy NJ. Earlystage leaking pipes GPR monitoring via microwave tomographic inversion. *J Appl Geophys* 2009;67(4):270–7.
- [11] Crocco L, Soldovieri F, Millington T, Cassidy NJ. Bistatic tomographic GPR imaging for incipient pipeline leakage evaluation. *Prog Electromagn Res* 2010;101:307–21.
- [12] Schneider WA. Integral formulation for migration in two and three dimensions. *Geophysics* 1978;43:49–76.
- [13] Gazdag J. Wave equation migration with the phase-shift method. *Geophysics* 1978;43:1342–51.
- [14] Claerhout JF, Doherty SM. Downward continuation of move out-corrected sesimograms. *Geophysics* 1972;37:741–68.
- [15] Cafforio C, Prati C, Rocca F. SAR data focusing using seismic migration techniques. *IEEE T Geosci Remote* 1991;27:194–207.
- [16] Ozdemir C, Demirci S, Yigit E. Practical algorithms to focus B-scan GPR images: theory and application to real data. *Prog Electromagn Res B-PIER B* 2008;6:109–22.
- [17] Yigit E, Demirci S, Ozdemir C, Kavak A. A synthetic aperture radar-based focusing algorithm for B-scan ground penetrating radar imagery. *Microw Opt Technol Lett* 2007;49:2534–40.
- [18] Miller D, Oristaglio M, Beylkin G. A new slant on seismic imaging: Migration and integral geometry. *Geophysics* 1987;52:943–64.
- [19] Ozdemir C, Demirci S, Yigit E, Kavak A. A hyperbolic summation method to focus B-scan ground penetrating radar images: an experimental study with a stepped frequency system. *Microw Opt Technol Lett* 2007;49(3):671–6.
- [20] Carin L, Geng N, McClure M, Sichina J, Nguyen L. Ultra-wide-band synthetic-aperture radar for mine-field detection. *IEEE Antennas Propag* 1999;41(1):18–33.
- [21] Cui G, Kong L, Yang J. A back-projection algorithm to stepped-frequency synthetic aperture through-the-wall radar imaging. In: *Process of First Asian and Pacific Conference on Synthetic Aperture Radar-APSAR 2007*, Huangshan, China, November 5–9, 2007, p. 123–6.
- [22] Halman JI, Shubert KA, Ruck GT. SAR processing of ground-penetrating radar data for buried UXO detection: results from a surface-based system. *IEEE T Antenn Propag* 1998;46(7):1023–7.
- [23] Lei W, Su Y, Huang CLA. TAM-BP imaging algorithm in GPR application. In: *Proceedings of the Fourth International Conference on Microwave and Millimeter Wave Technology-ICMMT*, Beijing, China, August 18–21, 2004, p. 619–21.
- [24] Vitebskiy S, Carin L, Ressler MA, Le FH. Ultra-wideband, short-pulse ground-penetrating radar: simulation and measurement. *IEEE T Geosci Remote* 1997;35(3):762–72.
- [25] Zhou L, Su Y. GPR imaging algorithm with artifacts suppression. In: *Proceedings of the Thirteenth International Conference on Ground Penetrating Radar (GPR) 2010*, Lecce, Italy, June 21–25, 2010, p. 1–7.
- [26] Munson DC, O'Brien JD, Jenkins WK. A tomographic formulation of spotlight-mode synthetic aperture radar. *P IEEE* 1983;71(8):917–25.
- [27] Soldovieri F, Solimene R, Pierri R. A simple strategy to detect changes in through the wall imaging. *Prog Electromagn Res M* 2009;7:1–13.
- [28] Cooper GRJ, Cowan DR. Comparing time series using wavelet-based semblance analysis. *Comput Geosci-UK* 2008;34(2):95–102.
- [29] Daniels DJ. *Surface penetrating radar*. London: IEE Press; 1996.
- [30] Ozdemir C. *Synthetic aperture radar*. In: Chang K, editor. *The wiley encyclopedia of RF and microwave engineering*. New York: Wiley-Interscience; 2005. p. 5067–80.
- [31] Mersereau R, Oppenheim A. Digital reconstruction of multidimensional signals from their projections. *P IEEE* 1974;62(10):1319–38.
- [32] Huisman JA, Sperl C, Bouten W, Verstraten JM. Soil water content measurements at different scales: accuracy of time domain reflectometry and ground-penetrating radar. *J Hydrol* 2001;245(1–4):48–58.
- [33] <<http://lcs.syr.edu/faculty/lewalla/wavelets/morlet.pdf>>.